PCCP

ROYAL SOCIETY OF CHEMISTRY

PAPER

View Article Online
View Journal | View Issue

Cite this: *Phys. Chem. Chem. Phys.*, 2026, **28**, 1132

Internal bridging engineering of NiO_x/Me-4PACz *via* selective guanidine-based hydrochlorides for efficient and stable inverted perovskite solar cells

Jiaqi Wang,*[a] Zhirui Chen,[a] Ye Song,[b] Chang Li,[cd] Caixuan Wang,[e] Jingjing Hui,[f] Junyu Nie,[a] Yi Wang,[a] Zhihai Cheng,[cd] Qi Li[f] and Cheng Mu*[a]

Received 26th July 2025,
Accepted 7th November 2025

DOI: 10.1039/d5cp02853a

rsc.li/pccp

The introduction of self-assembled molecular layers (SAMs) has recently brought breakthroughs to inverted perovskite solar cells (PSCs). Among them, the NiO_x/Me-4PACz hole transport layer (HTL) system exhibits remarkable potential for enhancing device performance. However, Me-4PACz suffers from inherent limitations, including uneven distribution, poor wettability with perovskite solution and limited stability. In this study, we introduce metformin hydrochloride (MFCl) and triaminoguanidine hydrochloride (TGCl) as internal molecular "bridges" between NiO_x and Me-4PACz to address these issues. This strategy aims to enhance charge transport, strengthen the interfacial anchoring between NiO_x and Me-4PACz, regulate the molecular organization of Me-4PACz, and optimize the buried interface. As a result, the crystallinity and quality of the perovskite layer are significantly improved, leading to enhanced device performance. The power conversion efficiency (PCE) of the modified device increases notably from 20.45% to 23.11% (MFCl) and 23.06% (TGCl), along with substantial improvements in operational stability.

Introduction

Inverted perovskite solar cells (PSCs) have attracted considerable attention due to their simplified architecture, low-temperature solution processability, negligible hysteresis, and compatibility with flexible substrates and all-perovskite tandem devices.[1,2] Nickel oxide (NiO_x) is widely employed as a hole transport layer (HTL) in inverted PSCs, attributed to its low cost, high optical transparency, and excellent stability.[3,4] However, NiO_x suffers from insufficient interfacial contact with the perovskite layer, which hampers charge transfer and limits crystal growth, ultimately degrading device performance.[5–9] To address these interfacial issues, self-assembled monolayers (SAMs) have emerged as a promising interfacial engineering strategy. Recent advancements in SAMs have enabled significant improvements in inverted PSCs by mitigating interfacial defects and enhancing energy level alignment. Notable SAMs include 2PACz,[10–12] MeO-2PACz,[13,14] Br-2PACz,[15,16] and Me-4PACz.[17] These molecules offer molecular-level control over interface properties and have been instrumental in overcoming the intrinsic limitations of NiO_x-based HTLs. For example, You *et al.* enhanced the uniformity and conductivity of NiO_x/Me-4PACz layers by introducing hydrogen peroxide, promoting Ni^{3+} formation and hydroxylation to strengthen surface bonding.[18] Li *et al.* employed *p*-phenylene diphosphonic acid (*p*-XPA) as an interfacial modifier, improving surface smoothness and reducing non-radiative recombination, achieving a certified power conversion efficiency (PCE) of 25.45%.[19] More recently, Chen *et al.* developed a mixed SAM system (NA-Me) by co-assembling Me-4PACz with a polycarboxylic aromatic compound, yielding a certified PCE of 26.69%.[20] Despite these advances, Me-4PACz still faces challenges such as agglomeration, uneven surface coverage,[20–23] and poor wettability with the perovskite solution.[17,24] These factors degrade the buried interface and compromise device efficiency. Furthermore, the interfacial interaction between SAMs and NiO_x remains weak, affecting the long-term stability of the device due to the heterogeneous distribution and incomplete coverage of SAMs.[25,26]

To overcome these limitations, we introduce guanidine-derived compounds as an interfacial layer between NiO_x and Me-4PACz. Although guanidinium salts are frequently

[a] *Key Laboratory of Advanced Light Conversion Materials and Biophotonics, Department of Chemistry, School of Chemistry and Life Resources, Renmin University of China, Beijing, 100872, P. R. China. E-mail: cmu@ruc.edu.cn*
[b] *SINOPEC Research Institute of Petroleum Processing, Beijing, 100083, P. R. China*
[c] *Key Laboratory of Quantum State Construction and Manipulation (Ministry of Education), Renmin University of China, Beijing, 100872, P. R. China*
[d] *Beijing Key Laboratory of Optoelectronic Functional Materials & Micro-nano Devices, Department of Physics, Renmin University of China, Beijing, 100872, P. R. China*
[e] *National Center for Nanoscience and Technology, Beijing, 100190, P. R. China*
[f] *College of Chemistry and Molecular Engineering, Peking University, Beijing 100871, P. R. China*

employed as additives in perovskite precursor solutions,[27–31] their application in interfacial engineering remains comparatively limited. In this study, metformin hydrochloride (MFCl) and triaminoguanidine hydrochloride (TGCl), both rich in guanidine and amine groups, are incorporated to strengthen the interaction between Me-4PACz and NiO_x. This strategy modulates the growth of Me-4PACz, reduces surface roughness, improves buried interface quality, and enhances perovskite crystallinity. Devices modified with MFCl and TGCl exhibit significantly improved PCEs of 23.11% and 23.06%, respectively, compared to 20.43% for the control. Long-term stability is also enhanced: after 1800 h of storage at 20 °C in nitrogen, the MFCl- and TGCl-modified devices retained 97% and 94% of their initial efficiency, respectively. When stored at 65 °C for 1000 h, the PCE remained at 97% and 96%, respectively, demonstrating excellent thermal and operational stability.

Experimental

Materials

Patterned indium tin oxide (ITO) substrates were purchased from Opv Tech New Energy Technology Co., Ltd. Lead(II) iodide (PbI_2, 99.999%) and NiO_x nanoparticles (99.5%) were obtained from Advanced Election Technology Co., Ltd. Formamidinium iodide (FAI, 99.5%), methylammonium iodide (MAI, 99.5%), methylammonium chlorine (MACl, 99.5%), ethanediamine dihydroiodide (99.5%, EDADI), buckminsterfullerene (C_{60}, 99%), cesium iodide (CsI, 99.99%), and bathocuproine (BCP, 99%) were provided by Xi'an Yuri Solar Co., Ltd. Chlorobenzene (CB, 99.8%), isopropanol (IPA, 99.8%), *N*,*N*-dimethylformamide (DMF, 99.8%), and dimethyl sulfoxide (DMSO, 99.9%) were procured from Beijing J&K Technology Co., Ltd. Me-4PACz (>98%) was purchased from TCI Corporation. Metformin hydrochloride (MFCl, 99%) was purchased from Shanghai Xian Ding Biotechnology Co. Ltd, and triaminoguanidine hydrochloride (TGCl, 98%) was purchased from Macklin Biochemical Technology Co., Ltd, and guanidinium thiocyanate (GuaSCN ≥ 99%) was purchased from Aladdin Biochemical Technology Co., Ltd.

Solution preparation

Perovskite precursor solutions (1.67 M $Cs_{0.05}MA_{0.1}FA_{0.85}PbI_3$) were prepared by dissolving 21.63 mg CsI, 26.5 mg MAI, 243.63 mg FAI, and 807.3 mg PbI_2 in 1 mL of a mixed solvent of DMF and DMSO (828 μL DMF + 172 μL DMSO). Additionally, 16.63 mg MACl and 0.1 mg of GuaSCN were added to improve the quality of the perovskite films.

PSC fabrication

ITO substrates were cleaned by ultrasonication in a mixture of dishwashing detergent and deionized water for 30 minutes to remove oil residues, followed by sequential ultrasonication in acetone and IPA for 30 min. After drying at 65 °C for 2 h, the substrate was treated with UV/O_3 plasma for 5 min. A NiO_x nanoparticle solution (10 mg mL^{-1} in deionized water) was sonicated for 20 min and spin-coated onto the ITO substrates at 3000 rpm for 30 s, and then annealed at 150 °C for 30 minutes. For surface modification, MFCl or TGCl (dissolved in deionized water) was spin-coated onto the NiO_x film at 5000 rpm for 30 s and annealed at 150 °C for 30 min. The treated substrates (ITO/NiO_x, ITO/NiO_x/MFCl, or ITO/NiO_x/TGCl) were then transferred into an N_2-filled glovebox for further processing. Me-4PACz was dissolved in IPA (0.5 mg mL^{-1}) and spin-coated onto a NiO_x film at 3000 rpm for 30 s, followed by annealing at 100 °C for 10 min. Perovskite films were fabricated using a two-step spin-coating process: 1000 rpm for 10 s, followed by 5000 rpm for 35 s. During the second step, 150 μL CB was dropped as an antisolvent over 15 s near the end of the spin cycle. The films were then annealed at 120 °C for 10 min. Subsequently, a solution of EDADI (1 mg mL^{-1} in IPA: CB = 1 : 1 v/v) was spin-coated at 4500 rpm for 25 s and annealed at 100 °C for 5 min. Finally, C_{60} (26 nm), BCP (6 nm), and Ag (100 nm) layers were deposited using a thermal evaporation meter (FS-450, Fangsheng).

Characterization

The chemical interactions among NiO_x, MFCl, TGCl, and Me-4PACz were characterized by Fourier transform infrared spectroscopy (FTIR, Bruker Tensor 27) and X-ray photoelectron spectroscopy (XPS, Thermo Fisher Nexsa). Surface morphology was observed *via* scanning electron microscopy (SEM, Hitachi SU8010) and atomic force microscopy (AFM, Park NX10), including Kelvin probe force microscopy (KPFM). Elemental distribution was determined *via* energy-dispersive X-ray spectroscopy (EDS, Bruker XFlash 6160). Crystallinity was assessed by X-ray diffraction (XRD, Shimadzu XRD-7000), and ultraviolet photoelectron spectroscopy (UPS) was performed using a Thermo Fisher ESCALAB 250Xi. Photoluminescence (PL) spectroscopy was conducted using an FS5 fluorescence spectrophotometer, and time-resolved PL (TRPL) spectra were recorded using an FLS980 fluorescence spectrophotometer. Current density–voltage (*J*–*V*) characteristics were measured under AM 1.5G simulated solar illumination with a Keithley 2400 SourceMeter (active area: 0.1 cm^2). The external quantum efficiencies (EQEs) were tested using an EnliTech QE-R instrument. Space-charge-limited current (SCLC) and dark *J*–*V* curves were measured by the same Keithley 2400 SourceMeter under dark conditions. Electrochemical impedance spectroscopy (EIS) was performed using an electrochemical workstation (pp211, Zahner) in the frequency range from 1 to 10^6 Hz. Transient photovoltage (TPV) measurements were conducted using a nanosecond (ns)-pulsed beam (InnoLas, P1515; excitation wavelength: 355 nm; pulse width: 800 ps) and an oscilloscope (Lecroy, HDO4054A).

Results and discussion

Fig. 1a shows the molecular structure of MFCl and TGCl and a schematic illustration of the MFCl- or TGCl-modified HTL fabrication process. To verify that IPA didn't rinse MFCl and TGCl away, solubility tests were conducted. As shown in Fig. S1, IPA solutions containing 1 mg mL^{-1} MFCl and TGCl were prepared and thoroughly shaken for 5 minutes using a vortex

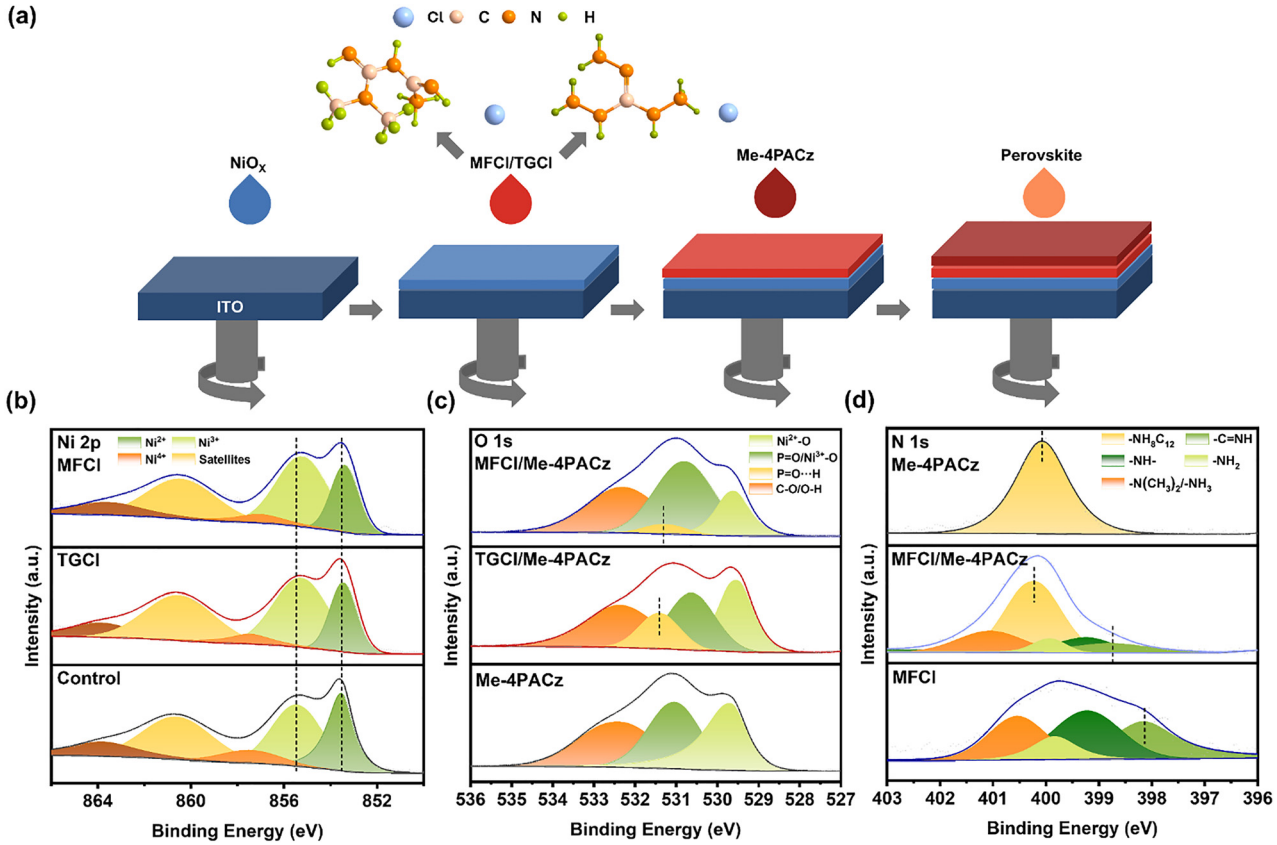

Fig. 1 (a) A schematic diagram of the fabrication process of MFCl and TGCl introduced between NiO_x and Me-4PACz. (b) XPS spectra of Ni 2p core levels for control, TGCl, and MFCl modified NiO_x films, respectively. (c) XPS spectra of O 1s core levels for control, TGCl, and MFCl modified Me-4PACz films, respectively. (d) XPS spectra of N 1s core levels for the MFCl film, Me-4PACz film and MFCl modified Me-4PACz film, respectively.

shaker. After standing, the residual MFCl and TGCl in the solutions could be clearly observed, indicating their low solubility in IPA. Furthermore, EDS was performed on films sequentially spin-coated with MFCl (or TGCl) aqueous solution and IPA solution (Fig. S2). The presence of C, N and Cl elements on both film surfaces confirmed that MFCl and TGCl existed on the samples. Although both TGCl and MFCl contain guanidinium moieties capable of interacting with NiO_x and Me-4PACz, their molecular structures lead to different interfacial modification behaviors. TGCl, featuring a single guanidine group, primarily offers multiple hydrogen bonding sites. In contrast, MFCl possesses a biguanide structure forming an extended, planar π-conjugated system. This structural distinction is pivotal, as the biguanide unit not only participates in hydrogen bonding but also enables strong π–π stacking interactions with the carbazole moiety of Me-4PACz, as will be discussed in the following analysis. We first investigated how guanidine hydrochloride interacts with the NiO_x and Me-4PACz layers by performing XPS on the NiO_x films before and after MFCl or TGCl treatment. The results for the Ni 2p region are presented in Fig. 1b and Table S1. The relative content and peak positions of Ni in various valence states are detailed in Table S1. In NiO_x, Ni^{3+}—associates its p-type characteristics and aids hole transport.[18,32] Upon treatment, the Ni 2p peaks shift to lower binding energy, indicating an increase in electron density around Ni atoms. Quantitatively, the Ni^{3+} fraction rises from 46.95% (control) to 58.48% (TGCl) and 62.50% (MFCl). Molecular structure analysis indicates that the guanidine moiety coordinates Ni^{3+}, stabilizing its high valence state and suppressing its reduction; MFCl's biguanide groups strengthen this effect even further. Meanwhile, TGCl's mild reducibility converts some Ni^{4+} to Ni^{3+}, boosting the Ni^{3+} content. FTIR (Fig. S3) confirms these coordination interactions: the C=N stretching vibration peaks of both TGCl and MFCl shift by 4.1 cm^{-1} and 8.3 cm^{-1}, respectively, demonstrating a stronger coordination interaction and corroborating the findings from XPS. Additionally, both modifiers smooth the NiO_x surface (Fig. S4), improving its contact with self-assembled monolayers (SAMs) and enhancing hole transport.

Next, we probed guanidine hydrochloride's effect on Me-4PACz by recording XPS spectra of O 1s and P 2p regions (Fig. 1c and Fig. S5). In films pretreated with MFCl or TGCl, the P=O peak splits into components 531.32 eV and 531.42 eV, consistent with hydrogen bonding between guanidine-NH_2 groups and the P=O moieties in Me-4PACz. TGCl-treated films display more pronounced peaks and shifts in binding energies, reflecting their higher $-NH_2$ content and stronger H-bonding. The P 2p peaks also shift slightly to lower binding energy (TGCl: 0.34 eV; MFCl: 0.06 eV), indicating an altered phosphorus chemical environment and an increase in the electron density. FTIR spectra (Fig. S6) corroborate this finding, showing

downshifts of the P═O stretching band by 9.7 cm^{-1} for MFCl and 21 cm^{-1} for TGCl, confirming that the hydrogen bonding interactions during interfacial modification are predominantly influenced by the P═O group.

In addition, considering the presence of a biguanide moiety in MFCl and a carbazole moiety in Me-4PACz, we explored the possibility of a specific interaction between them. As shown in Fig. 1d, XPS N1s analysis reveals that, after MFCl treatment, the binding energy of the nitrogen in the carbazole unit of Me-4PACz shifts from 400.08 eV to 400.23 eV. Moreover, compared with the single MFCl film, the peak corresponding to C═N in the MFCl film coated with Me-4PACz shifts from 398.14 eV to 398.74 eV, indicating a potential π–π stacking interaction between the biguanidino and carbazole moieties. This interaction may contribute to a more uniform distribution of Me-4PACz layers and mitigate its aggregation tendency. The FTIR spectra show that a new peak at 1568.8 cm^{-1} appeared in MFCl after the interaction with Me-4PACz, and it is absent in TGCl. This indicates that the peak is unlikely to arise from a hydrogen bond, but rather from a π–π stacking interaction between biguanide and carbazole units (Fig. S7). This π–π interaction serves as a key distinguishing feature, which likely guides a more planar and ordered arrangement of the Me-4PACz layer. This mechanistic contrast highlights that while TGCl effectively anchors the layer *via* hydrogen bonding, MFCl goes a step further by leveraging a synergy combination of hydrogen bonding and π–π stacking, thereby imparting a higher degree of structural order to the SAM distribution.

Next, we performed a series of characterizations on the Me-4PACz films. The surface morphologies of NiO_x/Me-4PACz, NiO_x/TGCl/Me-4PACz and NiO_x/MFCl/Me-4PACz films were analyzed using AFM (Fig. 2a–c). The root-mean-square (RMS)

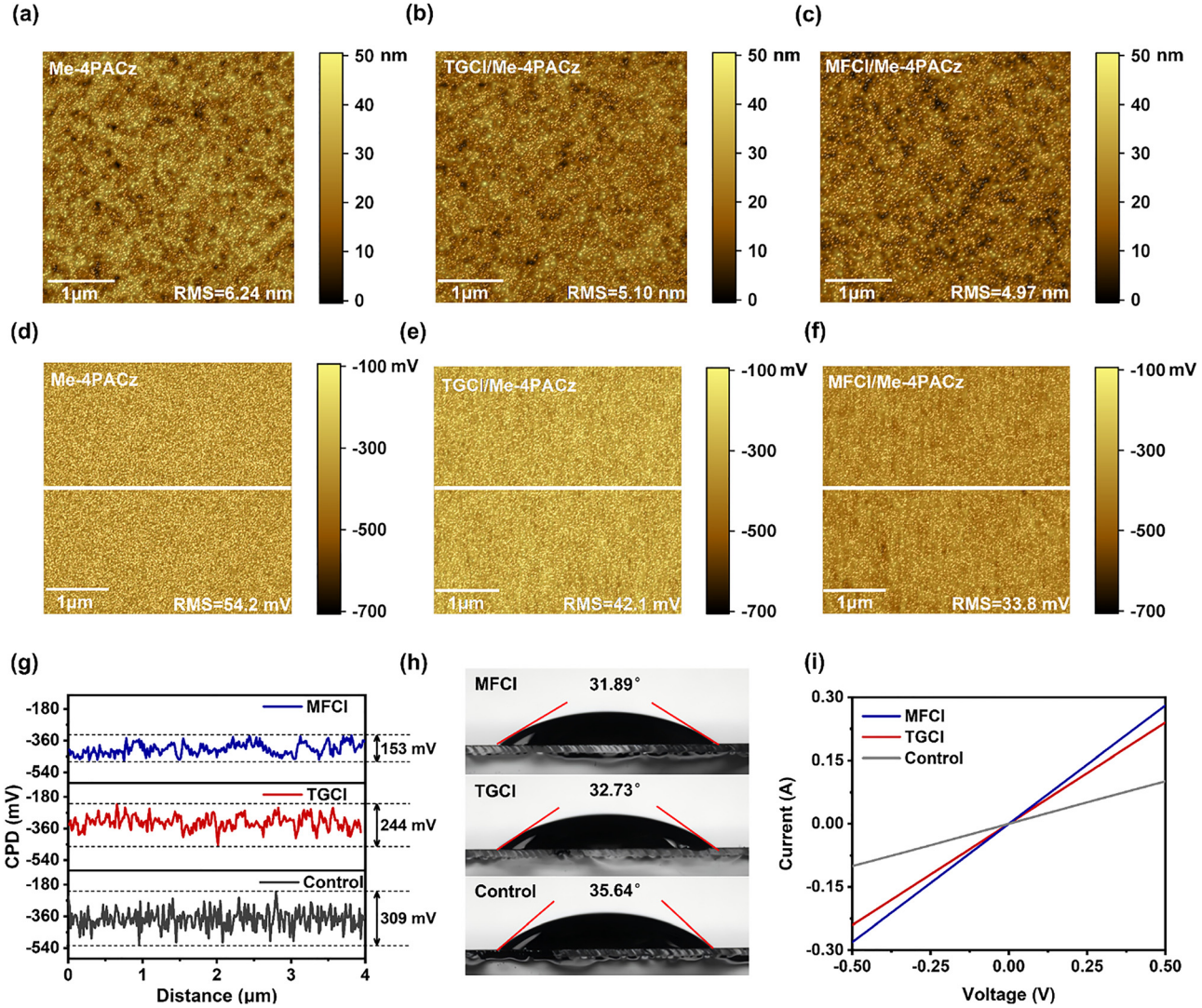

Fig. 2 The AFM images of the (a) Me-4PACz, (b) TGCl modified Me-4PACz film and (c) MFCl modified Me-4PACz film, respectively. KPFM images of the (d) Me-4PACz, (e) TGCl modified Me-4PACz film and (f) MFCl modified Me-4PACz film, respectively. (g) Corresponding line profiles the Me-4PACz, TGCl, and MFCl-modified Me-4PACz film, respectively. (h) Contact angles of the perovskite precursor solution on different HTL layers, respectively. (i) Conductivity of control, TGCl, and MFCl modified HTL, respectively.

roughness decreases from 6.24 nm (control) to 5.10 nm (TGCl) and 4.97 nm (MFCl). This reduction in surface roughness upon guanidino hydrochloride treatment is likely due to hydrogen bonding interactions, while the more pronounced smoothing effect observed for MFCl is attributed to the additional coordination effect of π–π stacking induced by the biguanide group. The significant decrease in roughness indicates a more uniform HTL surface, which improves the contact with the perovskite layer, facilitates more uniform perovskite crystallization, enhances film quality, and reduces defect formation.[19] Furthermore, KPFM was performed to evaluate the surface potential distribution of the three types of films (Fig. 2d–g). Compared with the control, the guanidinium hydrochloride treated films exhibited higher surface potential, lower work function and narrower, more uniform surface potential distribution. The RMS values of surface potential variation decreased from 54.2 mV (control) to 42.1 mV (TGCl) and 33.8 mV (MFCl), suggesting a reduced energetic disorder at the surface.[18,19] This effect is further confirmed by the surface potential line profiles (Fig. 2g), where the contact potential difference (ΔCPD) dropped markedly from 309 mV (control) to 244 mV (TGCl) and 153 mV (MFCl). Based on the above results, the TGCl treatment yielded a significant improvement over the control, effectively reducing both the RMS roughness and energetic disorder, thereby validating the effectiveness of hydrogen-bonding interface modification. However, the MFCl-treated film achieved the optimal state, exhibiting the lowest RMS roughness and the most uniform surface potential distribution. This clearly represents a structure–function correlation: the extended planar structure of MFCl's biguanide group, enabling π–π stacking, is responsible for the superior smoothness and electronic uniformity. This ultra-uniform substrate template facilitates the subsequent growth of high-quality perovskite films featuring larger grains and fewer defects, which is the key reason for the champion device performance of MFCl-based devices, especially raising the open-circuit voltage. Contact angle measurements of the three HTL films with the perovskite

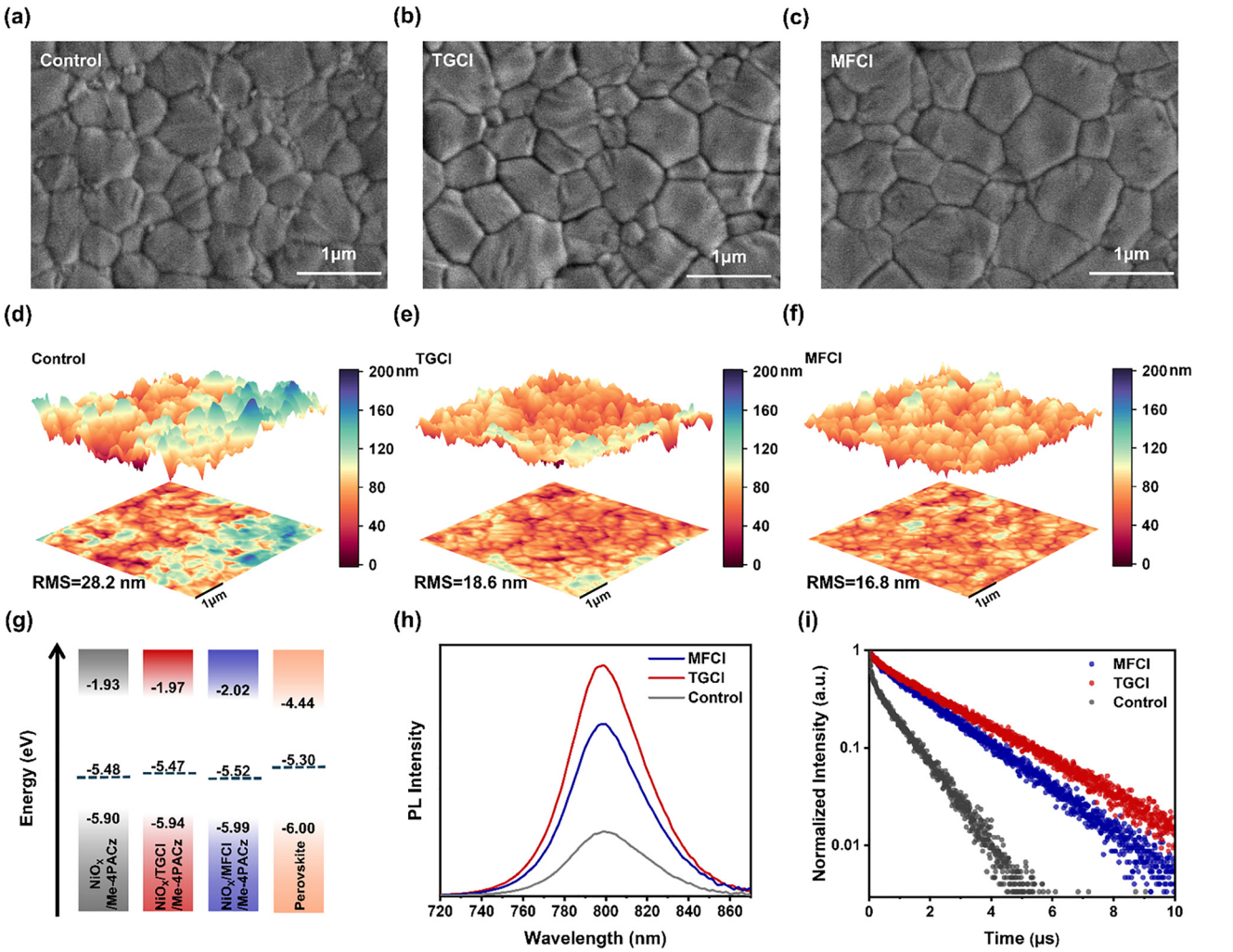

Fig. 3 Top-view SEM images (scale = 1 μm) of the (a) control, (b) TGCl modified perovskite film, and (c) MFCl modified perovskite film, respectively. AFM images of the (d) control, (e) TGCl modified perovskite film and (f) MFCl modified perovskite film, respectively. (g) Energy diagram for NiO_x/Me-4PACz, NiO_x/TGCl/Me-4PACz and NiO_x/MFCl/Me-4PACz compared with the perovskite. (h) PL and (i) TRPL of the control, TGCl modified and MFCl modified perovskite film, respectively.

precursor solution (Fig. 2h) showed improved wettability after guanidinium hydrochloride treatment, as evidenced by the reduced contact angles. This enhancement in surface wettability supports more uniform perovskite film formation and reduces buried interface defects. To investigate the effect of guanidinium hydrochloride on the charge transfer, we assessed conductivity using ITO/HTL/Ag device structures (Fig. 2i). The treated films exhibited enhanced conductivity, which is attributed to the increased Ni^{3+} content and the smoother, more uniform HTL surface. These improvements collectively facilitate more efficient hole transport and reduce charge accumulation at the HTL/perovskite interface.

To investigate the influence of guanidinium hydrochloride treatment on perovskite films, we comprehensively analyzed their morphology, crystal structure, energy level alignment and optical properties. The morphology of the perovskite films was characterized by SEM and AFM. As shown in Fig. 3a–c and Fig. S8, treatment with guanidine hydrochloride resulted in larger and more uniformly distributed perovskite grains. The average grain size increased from 0.46 μm (control) to 0.53 μm (TGCl) and 0.54 μm (MFCl). As illustrated in Fig. 3d–f, the surface roughness of the perovskite films decreased significantly, with the RMS roughness reducing from 28.2 nm in the control to 18.6 nm for TGCl-treated films and 16.8 nm for MFCl-treated films. A smoother surface enhances the contact between the perovskite layer and the underlying charge transport layers, promoting more efficient electron extraction and transfer. Cross-sectional SEM analysis was also conducted to further examine the device architectures (Fig. S9). The thickness of the perovskite layer was consistent across all three devices, measuring approximately 750 nm. Notably, the control device exhibited the presence of voids both at the buried interface of the perovskite layer and within the perovskite. In contrast, the device treated with guanidine-based hydrochlorides showed no obvious voids and displayed intimate contact between the perovskite and the HTL, indicating improved quality of the buried interface and a denser perovskite morphology. These structural features are advantageous for minimizing defect density, suppressing non-radiative recombination, and ultimately enhancing device performance. To further evaluate the effect of guanidine hydrochloride treatment on perovskite crystallinity, XRD analysis was performed (Fig. S10 and S11). The full width at half maximum (FWHM) of the (100) peak decreased after treatment, indicating improved crystallinity. Moreover, the peak corresponding to PbI_2 disappeared, suggesting suppression of residual lead iodide and enhanced phase purity.

Treatment of the HTL with guanidine hydrochloride significantly affects the energy level alignment at the buried perovskite interface. As illustrated in Fig. 3g and Fig. S12, UPS reveals a downward shift in the valence band maximum (E_{VBM}) of the HTL after guanidine hydrochloride treatment. This shift reduces the energy offset (ΔE) between the valence band maximum (VBM) of the perovskite and the highest occupied molecular orbital (HOMO) of the HTL, where $\Delta E = E_{VBM\text{-}HTL} - E_{VBM\text{-}PSK}$. The ΔE value decreases from 0.10 eV in the control sample to 0.06 eV for TGCl-treated and 0.01 eV for MFCl-treated films, indicating a reduced energy barrier that facilitated more

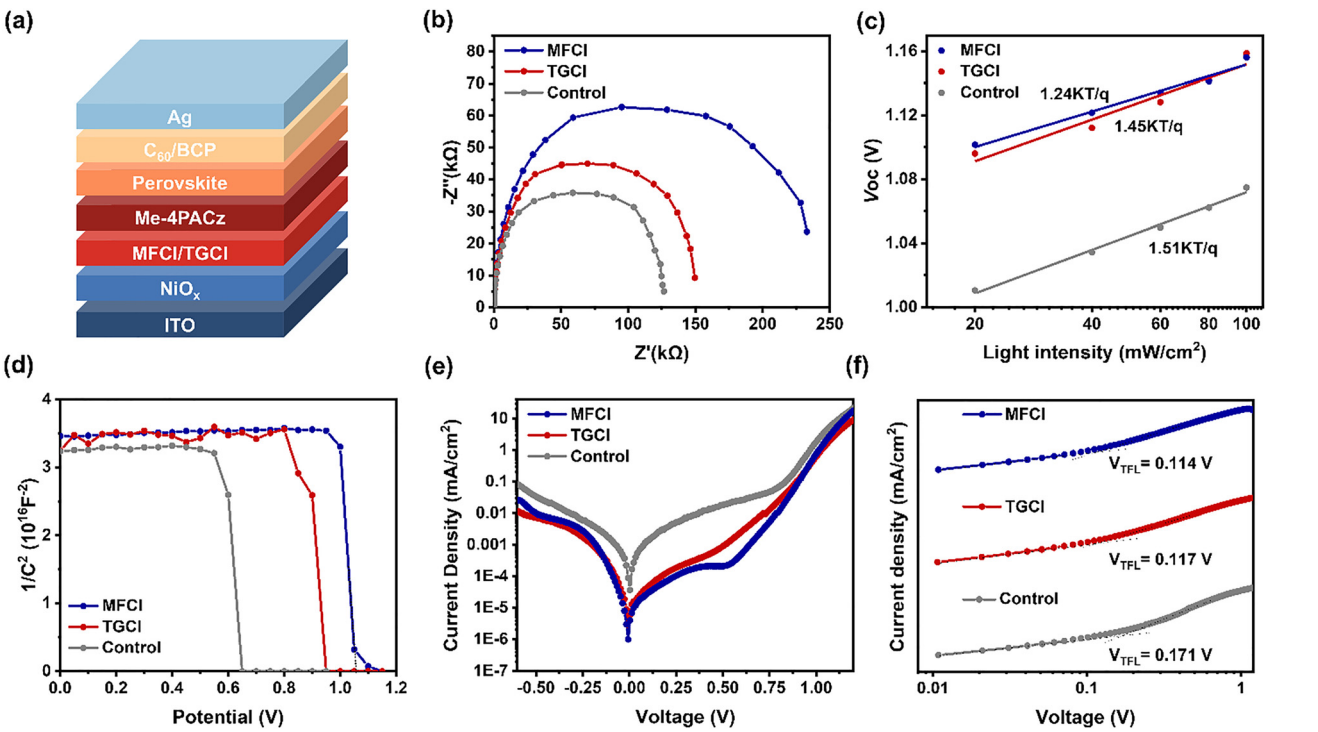

Fig. 4 (a) Complete structure of the device. (b) Nyquist plots. (c) Light intensity dependence of V_{OC} of PSCs. (d) Mott–Schottky plots. (e) Dark J–V measurements of different HTL layer-based inverted devices. (f) SCLC of the hole-only devices.

efficient hole extraction and minimized energy loss at the buried interface.

To further evaluate interfacial carrier recombination dynamics, steady-state PL and TRPL measurements were conducted. As shown in Fig. 3h–i and Table S2, perovskite films deposited on the guanidine hydrochloride-modified HTL exhibit significantly enhanced PL intensity and prolonged carrier lifetimes compared to the control, suggesting reduced non-radiative recombination and lower defect densities at the interface. The fitted carrier lifetimes are 0.95 μs for the control, 2.51 μs for TGCl and 1.96 μs for MFCl. Interestingly, although the MFCl-treated film shows a slightly shorter carrier lifetime than TGCl, this indicates more efficient hole extraction due to the improved energy level alignment observed in Fig. 3g, further validating the beneficial role of MFCl in interfacial engineering.

We fabricated devices with the structure ITO/NiO_x/MFCl(TGCl)/Me-4PACz/Perovskite/C_{60}/BCP/Ag to investigate the influence of guanidine hydrochloride treatment (Fig. 4a). The charge transfer kinetics at the interface were studied by EIS (Fig. 4b). After guanidine hydrochloride treatment, the devices exhibited increased recombination resistance, indicating suppressed charge recombination. To further understand the recombination mechanisms, we examined the correlation between light intensity and open-circuit voltage (V_{OC}) (Fig. 4c). The slope of the fitted curve is determined by the following equation:

$$V_{OC} = \frac{nk_B T}{q} \ln(I)$$

where k_B is the Boltzmann constant, T is the absolute temperature, q is the elementary charge, I is the intensity of light, and n is the ideal factor.[33] After treatment with guanidine hydrochloride, the n value decreased from 1.51 (control) to 1.45 (TGCl) and 1.24 (MFCl), indicating reduced trap-assisted recombination and defect density, which contributes to the improved V_{OC} and fill factor (FF).

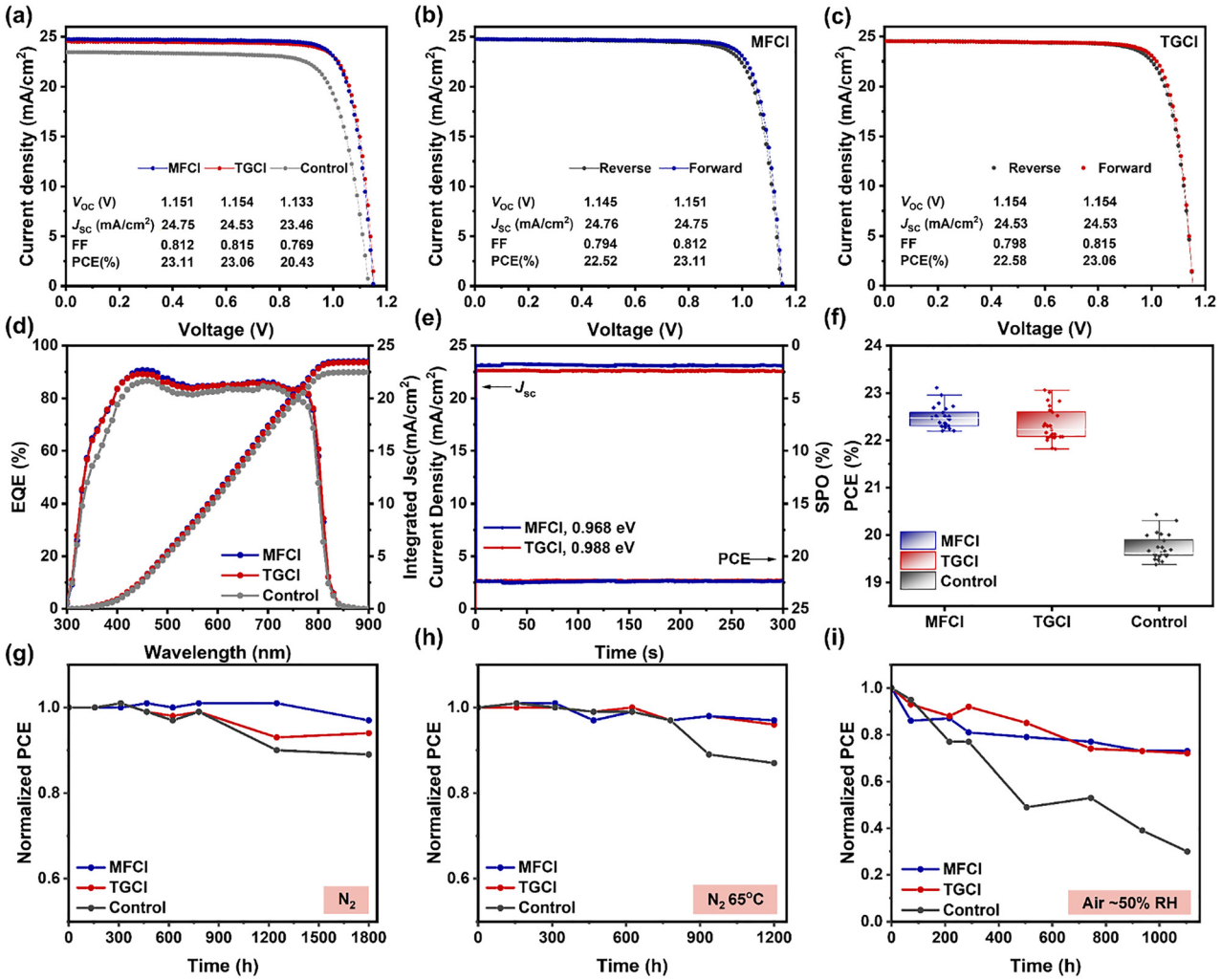

Fig. 5 (a) J–V curves of the control, TGCl, and MFCl modified HTL-based devices measured under AM 1.5G (100 mW cm^{-2}) illumination. J–V curves of the devices under reverse and forward scan for the (b) MFCl and (c) TGCl modified devices, respectively. (d) EQE of the control, TGCl, and MFCl modified devices, respectively. (e) The SPO of the TGCl and MFCl modified devices, respectively. (f) PCE statistics of 25 devices for the control, TGCl, and MFCl modified devices, respectively. (g) Stability of unencapsulated PSCs under an N_2 atmosphere. (h) Thermal stability of unencapsulated PSCs during 65 °C aging. (i) Humidity stability of unencapsulated PSCs under an air atmosphere.

Mott–Schottky analysis further revealed that the built-in potentials (V_{bi}) increased from 0.65 V (control) to 0.95 V (TGCl) and 1.06 V (MFCl) (Fig. 4d), suggesting enhanced carrier separation and transport efficiency. Dark *J–V* curves (Fig. 4e) indicated a significant reduction in the leakage current after guanidine hydrochloride treatment, attributed to improved Me-4PACz coverage on NiO_x, and reduced buried interface defects. To quantify defect density, the space charge limited current (SCLC) method was employed using ITO/NiO_x/(with or without MFCl or TGCl)/Me-4PACz/perovskite/Spiro-OMeTAD/Ag device (Fig. 4f). The trap-fill limit voltage (V_{TFL}) was extracted, and trap state densities (N_t) were calculated using the following equation:

$$N_t = \frac{2\varepsilon_r\varepsilon_0 V_{TFL}}{qL^2}$$

where ε_r is the relative dielectric constant, ε_0 is the vacuum permittivity, q is the electron charge, and L is the perovskite film thickness. Following treatment, N_t decreased from 1.37×10^{15} cm^{-3} (control) to 9.36×10^{14} cm^{-3} (TGCl) and 9.10×10^{14} cm^{-3} (MFCl), further confirming the suppression of defect-related recombination. To probe the carrier dynamics, transient photovoltage (TPV) measurements were performed. As illustrated in Fig. S13, the decay time extended from 0.088 ms for the control sample to 0.120 ms (TGCl) and 0.146 ms (MFCl). These results suggest that the guanidine-based hydrochloride treatment yields a lower defect density, which suppresses recombination and is critical for achieving a higher open-circuit voltage.

After optimizing the additive concentration, the best-performing concentrations were 1 mg mL^{-1} for MFCl and 0.2 mg mL^{-1} for TGCl (Tables S3 and S4). As shown in Fig. 5a–c, the champion MFCl-modified device achieved a PCE of 23.11% (J_{SC} = 24.75 mA cm^{-2}, V_{OC} = 1.151 V, FF = 0.812), while the TGCl-modified device yielded a PCE of 23.06% (J_{SC} = 24.53 mA cm^{-2}, V_{OC} = 1.154 V, FF = 0.815). In contrast, the control device showed a PCE of 20.43% (J_{SC} = 23.46 mA cm^{-2}, V_{OC} = 1.133 V, FF = 0.769). Fig. 5d presents the EQE spectra, with integrated J_{SC} values of 22.48 mA cm^{-2} for control, and enhanced values of 23.41 mA cm^{-2} (TGCl) and 23.51 mA cm^{-2} (MFCl). The devices modified with TGCl and MFCl show steady state output (SPO) efficiency of 22.32% and 22.36%, with stabilized J_{SC} values of 22.59 mA cm^{-2} and 23.10 mA cm^{-2}, respectively (Fig. 5e). Statistical distributions of photovoltaic parameters for 25 devices (Fig. 5f and Fig. S14) reveal that guanidine hydrochloride treatment significantly enhances device performance. The increase in V_{OC} originates primarily from reduced defect density and suppressed nonradiative recombination. In contrast, the enhancement in J_{SC} arises from enhanced HTL conductivity, improved energy level alignment, and the inhibition of nonradiative recombination at interfaces. MFCl modified devices exhibited slightly higher J_{SC} and V_{OC} of MFCl than those treated with TGCl, along with narrower parameter distributions and better reproducibility, indicating superior overall performance.

Device stability was evaluated under various conditions. After 1800 h of storage at room temperature (20 °C) under an N_2 atmosphere, PCE retention was 97% (MFCl), 94% (TGCl), and 89% (control) (Fig. 5g). After 1000 h storage at 65 °C in N_2, the PCEs of MFCl and TGCl modified devices and control were 97%, 96% and 87% of the initial value, respectively (Fig. 5h). Under ambient air (20 °C, ~50% RH) for 1000 h, PCE retention was 73% (MFCl), 72% (TGCl) and only 30% (control) (Fig. 5i). These results clearly demonstrate the significant role of guanidine hydrochloride modification in enhancing device stability under inert, hot, and humid conditions.

Conclusions

In conclusion, we propose an interfacial engineering strategy by introducing a guanidine-based hydrochloride layer between NiO_x and Me-4PACz. The incorporation of MFCl and TGCl facilitates the increase of Ni^{3+} content in NiO_x through coordination interactions, thereby enhancing the conductivity of the HTL. Additionally, hydrogen bonding between guanidine-based hydrochlorides and adjacent layers improves interfacial adhesion and promotes the orderly growth of Me-4PACz, resulting in a smoother and more uniform surface. This optimized interface not only fosters improved contact between layers but also creates a favorable environment for the crystallization and carrier transport of perovskite films. Moreover, guanidine-based hydrochloride treatments effectively modify the energy level alignment of the HTL, reducing the interfacial energy barrier and achieving better energy levels matching with the perovskite layer. This alignment suppresses carrier accumulation at the buried interface and facilitates more efficient hole extraction and transport. Notably, MFCl utilizes its biguanide functional group to establish key π–π stacking interactions with the Me-4PACz layer. The combination of π–π stacking and hydrogen bonding promotes superior molecular ordering at the interface, which in turn facilitates the formation of a more uniform HTL. This structural improvement is critical for achieving optimal device efficiency for MFCl-based devices. Devices modified with MFCl achieve a champion PCE of 23.11%, while that of TGCl-modified devices reaches 23.06%, both representing significant improvements over the control group. Furthermore, the modified devices demonstrate excellent operational and storage stability under various environmental conditions. Overall, the use of guanidine hydrochloride as a molecular bridge between NiO_x and SAMs layers offers a promising approach for interface modification, enabling notable enhancements in both efficiency and long-term stability of inverted PSCs.

Author contributions

Jiaqi Wang: writing – original draft, validation, methodology, and data curation. Zhirui Chen: formal analysis. Ye Song: investigation. Chang Li: data curation. Caixuan Wang: investigation. Jingjing Hui: data curation. Junyu Nie: data curation. Yi Wang: supervision. Zhihai Cheng: supervision. Qi Li: supervision. Cheng Mu: writing – review & editing, validation, supervision, and funding acquisition.

Conflicts of interest

There are no conflicts to declare.

Data availability

The data supporting this article have been included as part of the supplementary information (SI). Supplementary information: XPS data (Ni 2p, P 2p); TRPL fitting parameter; key photovoltaic parameters of devices with different dopant concentrations; EDS patterns; FTIR results; AFM images of NiO_x-films; SEM images and XRD patterns of perovskite films; UPS results; TPV measurements; J_{SC}, V_{OC}, and FF statistic diagrams. See DOI: https://doi.org/10.1039/d5cp02853a.

Acknowledgements

This study was supported by the National Energy Green Hydrogen Refining Research & Development Center and Beijing Natural Science Foundation (2252009).

Notes and references

1 K. Feng, G. Wang, Q. Lian, S. Gámez-Valenzuela, B. Li, R. Ding, W. Yang, K. Wang, J. Zeng, Y. Zhang, S. Y. Jeong, B. Xu, A. Ho-Baillie, H. Y. Woo, A. Facchetti and X. Guo, *Nat. Mater.*, 2025, **24**, 770.
2 Q. Tan, Z. Li, G. Luo, X. Zhang, B. Che, G. Chen, H. Gao, D. He, G. Ma, J. Wang, J. Xiu, H. Yi, T. Chen and Z. He, *Nature*, 2023, **620**, 545.
3 Y. Yang, R. Chen, J. Wu, Z. Dai, C. Luo, Z. Fang, S. Wan, L. Chao, Z. Liu and H. Wang, *Angew. Chem., Int. Ed.*, 2024, **63**, e202409689.
4 Z. R. Marand, A. Kermanpur, F. Karimzadeh, E. M. Barea, E. Hassanabadi, E. H. Anaraki, B. Julián-López, S. Masi and I. Mora-Seró, *Nanomaterials*, 2020, **10**, 872.
5 J. Lin, Y. Wang, A. Khaleed, A. A. Syed, Y. He, C. C. S. Chan, Y. Li, K. Liu, G. Li, K. S. Wong, J. Popović, J. Fan, A. M. C. Ng and A. B. Djurišić, *ACS Appl. Mater. Interfaces*, 2023, **15**, 24437.
6 T. Wu, L. K. Ono, R. Yoshioka, C. Ding, C. Zhang, S. Mariotti, J. Zhang, K. Mitrofanov, X. Liu, H. Segawa, R. Kabe, L. Han and Y. Qi, *Energy Environ. Sci.*, 2022, **15**, 4612.
7 S. Wang, D. Khan, W. Zhou, Y. Sui, T. Zhang, G. Yu, Y. Huang, X. Yang, X. Chen, H. Yan, J. Tang, F. Yang, P. Han, Z. Zheng, Y. Zhang and Z. Tang, *Adv. Funct. Mater.*, 2024, **34**, 2316202.
8 Y. Liu, B. Ding, G. Zhang, X. Ma, Y. Wang, X. Zhang, L. Zeng, M. K. Nazeeruddin, G. Yang and B. Chen, *Adv. Sci.*, 2024, **11**, 2309111.
9 C. C. Boyd, R. C. Shallcross, T. Moot, R. Kerner, L. Bertoluzzi, A. Onno, S. Kavadiya, C. Chosy, E. J. Wolf, J. Werner, J. A. Raiford, C. de Paula, A. F. Palmstrom, Z. J. Yu, J. J. Berry, S. F. Bent, Z. C. Holman, J. M. Luther, E. L. Ratcliff, N. R. Armstrong and M. D. McGehee, *Joule*, 2020, **4**, 1759.
10 K. Zhao, Q. Liu, L. Yao, C. Değer, J. Shen, X. Zhang, P. Shi, Y. Tian, Y. Luo, J. Xu, J. Zhou, D. Jin, S. Wang, W. Fan, S. Zhang, S. Chu, X. Wang, L. Tian, R. Liu, L. Zhang, I. Yavuz, H.-F. Wang, D. Yang, R. Wang and J. Xue, *Nature*, 2024, **632**, 301.
11 Z.-R. Lan, D.-X. Ma, K. Tang, J. Yao, J.-Y. Shao and Y.-W. Zhong, *CCS Chem.*, 2025, **7**, 2672–2680.
12 Y. Tan, X. Chang, J.-X. Zhong, W. Feng, M. Yang, T. Tian, L. Gong and W.-Q. Wu, *CCS Chem.*, 2023, **5**, 1802.
13 Q. Jiang, R. Tirawat, R. A. Kerner, E. A. Gaulding, Y. Xian, X. Wang, J. M. Newkirk, Y. Yan, J. J. Berry and K. Zhu, *Nature*, 2023, **623**, 313.
14 X. Zhang, Y. Wang, K. Zhang, M. Tao, H. Guo, L. Guo, Z. Song, J. Wen, Y. Yang, Y. Hou and Y. Song, *Angew. Chem., Int. Ed.*, 2025, **64**, e202423827.
15 H. Xu, A. Sharma, J. Han, B. P. Kirk, A. R. Alghamdi, F. Xu, Y. Zhang, A.-H. Emwas, G. Hizalan, S. De Wolf, M. R. Andersson, G. G. Andersson and D. Baran, *Adv. Energy Mater.*, 2024, **14**, 2401262.
16 A. S. Subbiah, L. V. Torres Merino, A. R. Pininti, V. Hnapovskyi, S. Mannar, E. Aydin, A. Razzaq, T. G. Allen and S. De Wolf, *ACS Energy Lett.*, 2024, **9**, 727.
17 K. Hossain, A. Kulkarni, U. Bothra, B. Klingebiel, T. Kirchartz, M. Saliba and D. Kabra, *ACS Energy Lett.*, 2023, **8**, 3860.
18 S. Yu, Z. Xiong, H. Zhou, Q. Zhang, Z. Wang, F. Ma, Z. Qu, Y. Zhao, X. Chu, X. Zhang and J. You, *Science*, 2023, **382**, 1399.
19 X. He, H. Chen, J. Yang, T. Wang, X. Pu, G. Feng, S. Jia, Y. Bai, Z. Zhou, Q. Cao and X. Li, *Angew. Chem., Int. Ed.*, 2024, **63**, e202412601.
20 S. Liu, J. Li, W. Xiao, R. Chen, Z. Sun, Y. Zhang, X. Lei, S. Hu, M. Kober-Czerny, J. Wang, F. Ren, Q. Zhou, H. Raza, Y. Gao, Y. Ji, S. Li, H. Li, L. Qiu, W. Huang, Y. Zhao, B. Xu, Z. Liu, H. J. Snaith, N.-G. Park and W. Chen, *Nature*, 2024, **632**, 53.
21 S. Qu, F. Yang, H. Huang, Y. Li, C. Sun, Q. Zhang, S. Du, L. Yan, Z. Lan, Z. Wang, T. Jiang, P. Cui, X. Ai and M. Li, *Energy Environ. Sci.*, 2025, **18**, 318.
22 S. M. Park, M. Wei, N. Lempesis, W. Yu, T. Hossain, L. Agosta, V. Carnevali, H. R. Atapattu, P. Serles, F. T. Eickemeyer, H. Shin, M. Vafaie, D. Choi, K. Darabi, E. D. Jung, Y. Yang, D. B. Kim, S. M. Zakeeruddin, B. Chen, A. Amassian, T. Filleter, M. G. Kanatzidis, K. R. Graham, L. Xiao, U. Rothlisberger, M. Grätzel and E. H. Sargent, *Nature*, 2023, **624**, 289.
23 R. Guo, X. Wang, X. Jia, X. Guo, J. Li, Z. Li, K. Sun, X. Jiang, E. Alvianto, Z. Shi, M. Schwartzkopf, P. Müller-Buschbaum and Y. Hou, *Adv. Energy Mater.*, 2023, **13**, 2302280.
24 Q. Jiang and K. Zhu, *Nat. Rev. Mater.*, 2024, **9**, 399.
25 C. Li, Y. Chen, Z. Zhang, C. Liu, F. Guo, W. Ahmad and P. Gao, *Energy Environ. Sci.*, 2024, **17**, 6157.
26 S. Wang, H. Guo and Y. Wu, *Mater. Futures*, 2023, **2**, 012105.
27 W. Zhou, S. Tai, Y. Li, H. Fu and Q. Zheng, *Adv. Funct. Mater.*, 2024, **34**, 2407897.

28 L. Yan, H. Huang, P. Cui, S. Du, Z. Lan, Y. Yang, S. Qu, X. Wang, Q. Zhang, B. Liu, X. Yue, X. Zhao, Y. Li, H. Li, J. Ji and M. Li, *Nat. Energy*, 2023, **8**, 1158.
29 A. Mahapatra, R. Runjhun, J. Nawrocki, J. Lewiński, A. Kalam, P. Kumar, S. Trivedi, M. M. Tavakoli, D. Prochowicz and P. Yadav, *Phys. Chem. Chem. Phys.*, 2020, **22**, 11467.
30 S. Du, H. Huang, Z. Lan, P. Cui, L. Li, M. Wang, S. Qu, L. Yan, C. Sun, Y. Yang, X. Wang and M. Li, *Nat. Commun.*, 2024, **15**, 5223.
31 H. Dong, J. Qu, X. Yue, Y. Zhao, W. Wang, D. Chen, W. Zhu, H. Xi, L. Zhou, J. Zhang, G. Lu, C. Zhang and Y. Hao, *Adv. Energy Mater.*, 2025, **15**, 2403965.
32 S. Wang, Y. Li, J. Yang, T. Wang, B. Yang, Q. Cao, X. Pu, L. Etgar, J. Han, J. Zhao, X. Li and A. Hagfeldt, *Angew. Chem., Int. Ed.*, 2022, **61**, e202116534.
33 H. Zhang, X. Ren, X. Chen, J. Mao, J. Cheng, Y. Zhao, Y. Liu, J. Milic, W.-J. Yin, M. Grätzel and W. C. H. Choy, *Energy Environ. Sci.*, 2018, **11**, 2253.